### Title

Noncontact Electrical Permittivity Mapping and pH-Sensitive Films for Osseointegrated Prosthesis and Infection Monitoring.




### Journal

IEEE transactions on medical imaging, 36(11)

### ISSN

0278-0062



### Authors

Gupta, Sumit
Loh, Kenneth J



### Publication Date

2017-11-01

### DOI

10.1109/tmi.2017.2707390

Peer reviewed

# Noncontact Electrical Permittivity Mapping and pH-Sensitive Films for Osseointegrated Prosthesis and Infection Monitoring

Sumit Gupta, *Student Member*, *IEEE* and Kenneth J. Loh, *Member*, *IEEE*

***Abstract*—The objective of this study is to develop a noncontact, noninvasive system for detecting and monitoring subcutaneous infection occurring at the tissue and osseointegrated prosthesis interface. It is known that the local pH of tissue can change due to infection. Therefore, the sensing system integrates two parts, namely, pH-sensitive thin films that can be coated onto prosthesis surfaces prior to them being implanted and an electrical capacitance tomography (ECT) algorithm that can reconstruct the spatial permittivity distribution of a region of space in a noncontact fashion. First, a thin film pH sensor was fabricated by spray-coating, and tests confirmed that the film exhibited changes in its permittivity due to pH. Second, the ECT forward and inverse problems were implemented. Third, an aluminum rod was employed as a representative phantom of an osseointegrated prosthesis and then spray-coated with the pH sensor. Finally, the film-coated phantom was immersed in different pH buffers, dried, and subjected to ECT interrogation and spatial permittivity reconstruction. The results validated that ECT was able to detect and localize permittivity variations correlated to pH changes.**

***Index Terms*—Electrical capacitance tomography, infection, nanotube, noncontact, pH sensing, polyaniline, prosthesis, thin film**

## I. Introduction

According to a report published in the Archives of Physical Medicine and Rehabilitation in 2008 [1], more than 2 million people in the U.S. suffered from limb loss with ~ 185,000 amputations occurring each year [2]. It was estimated that 54% of these amputations were due to vascular diseases (*e.g.*, diabetes and peripheral arterial diseases), while 45% was a result of trauma [1]. In 2010, more than 950 U.S. soldiers lost their limbs due to combat-related amputations [3], followed by ~ 26% increase in 2012 due to amplified conflicts [4]. Overall, hospital costs associated with amputations were more than $8.3 billion per year [5]. Nevertheless, amputations are performed because of medical necessity. The main concern thereafter is how patients can regain functionality and quality of life.

Advances in prostheses enable amputees to resume their daily activities and enhance quality of life. Today, socket prostheses are most widely used. However, since the soft tissue of the residual stump makes direct contact with the socket, they often become compressed and deformed, which could cause skin problems (*e.g.*, pressure ulcers) and is a major drawback.

Osseointegration, whose application is well-established in dentistry [6], involves anchoring a portion of the prosthesis in bone and consists of a percutaneous element that is attached to the artificial limb. It is gaining popularity since it eliminates the dermatological issues of socket-based systems. In this method, the structural connection between the metallic fixture and bone is generally achieved either by screw fixation [7] or press-fit implantation [8]. Osseointegrated implants improve amputees' quality of life, sitting comfort, and gait [9]. However, the chances of a caustic microbial attack is still high, where some severe cases result in permanent disability and implant removal [10]. According to Branemark *et al*. [7], more than half of the population studied with transfemoral osseointegrated prostheses with screw-type fixtures contracted infection, which is a significant concern. In general, tissue that interfaces with the percutaneous abutment is highly susceptive to infection.

Acute infection, which generally occurs within the first three months post-surgery, is frequently caused by vitriolic bacterial attack by *S. aureus*. Infection due to less malicious bacteria (*e.g.*, *P. acnes*) causes serious issues after several months of osseo-integration. Symptoms of infection are severe pain, swelling, and erythema at the skin-abutment interface with mild to high fever, followed by prosthesis loosening and discharge with sinus tract formation. Purulent discharging fistula can develop at the prosthesis interfaces with the formation of cellulitis or tissue necrosis, which can impair mobility and prosthesis function [11]. Infection can also lead to gradual loosening and implant malposition with dislocation instability [12]. Thus, monitoring signs of infections and identifying regions of infection for early treatment are critical. Daily skin inspections can help detect anomalies that suggest infection. Superficial infections can be treated with appropriate oral antibiotics to resolve issues within a few weeks [8]. Unfortunately, infection can initiate subcutaneously and remain undetected for longer periods to cause severe complications. In these circumstances, a more detailed clinical assessment of the infected region is needed.

C-reactive protein is a high sensitivity, high specificity, preoperative blood test for detecting infection [13]. However, false positives often occur with patients previously treated with antimicrobial agents or subjected to less virulent bacterial attack

Manuscript received January 6, 2017; accepted on May 18, 2017. This research was supported by the U.S. Office of Naval Research under Contract No. N00014-17-1-2550. Partial support was also provided by the Jacobs School of Engineering, University of California-San Diego.

S. Gupta and K. J. Loh are with the Structural Engineering Department, University of California-San Diego, La Jolla, CA 92093 USA. Corresponding author e-mail: kenloh@ucsd.edu.

(*e.g. P. acnes*). Histopathological examination of periprosthetic tissues [14] and intraoperative microbiological testing [15] are two other methods used when microbiological tests are not performed preoperatively, but specimens need to be collected at the time of surgery with antimicrobial therapy suspended at least two weeks prior to the patient's surgery. Uncertainties associated with diagnosis of infection can be addressed by synovial-fluid test, but its sensitivity diminishes drastically if patients have had earlier microbial treatment [16].

Aside from the aforementioned methods, imaging can also be used for detecting infection. Plain radiography, computed tomography (CT), and magnetic resonance imaging (MRI) are three commonly adopted techniques. However, plain radiography suffers from low sensitivity with limited specificity [17]. Diagnosis of infection by CT or MRI is often hindered by artifacts produced by the prosthesis itself [11]. PET, or 18F-fluorodeoxyglucose positron-emission tomography, is an emerging imaging modality with higher sensitivity (~ 82%) and specificity (~ 87%) [18]. Scintigraphy with antigranulocyte monoclonal antibodies coupled with hybrid imaging is gaining popularity, but its merit is still under investigation [11].

Another potential sensing modality that one might be able to use for detecting infection is by monitoring changes in the biochemical environment in the human body. It has been found that infection caused by different microorganisms at the human-prosthesis interface influences the pH of infected cells. Sebaceous glands in the human body support the growth of *P. acnes*, which can hydrolyze the triglycerides present in sebum to release fatty acids and decrease the pH of infected cells to as low as ~ 5 [19]. On the other hand, infection associated with *S. aureus* is mainly due to their adhesion on the implanted prosthesis surface, which forms a biofilm and prohibits the penetration of antibiotics, resulting in chronic inflammation.

Therefore, the focus of this study is to devise a noncontact, noninvasive, imaging tool that can be used by physicians (or even patients) to accurately detect the early growth of subcutaneous infection occurring at the tissue-prosthesis interface. It is envisioned that the results from the proposed method can reduce the amount of unnecessary, complicated, expensive, and painful medical tests while facilitating diagnosis and use of appropriate infection treatment strategies. The proposed imaging technique is based on electrical capacitance tomography (ECT) and used in conjunction with embedded, passive, pH thin film sensors that exhibit changes in its dielectric property due to pH. First, ECT can reconstruct the spatial permittivity distribution of a predefined sensing domain using measured sets of capacitance obtained at electrodes surrounding a sensing domain. Second, since infection can alter the pH of tissue, a thin film pH sensor based on multi-walled carbon nanotubes (MWCNT) and polyaniline (PANI) was fabricated, where the film can exhibit dramatic permittivity changes due to different pH and then be imaged by ECT without making contact with the residual stump or prosthesis. This paper begins with the theoretical foundations of ECT, followed by a discussion of the experiments. Then, pH sensing and ECT test results are presented. Numerical simulations were also performed to assess the detection of changes in permittivity due to pH/infection.

## II. ECT Background

The spatial permittivity reconstruction technique used in this study is centered around the theory of a soft field imaging technique known as electrical capacitance tomography [20]. In general, a typical ECT system comprises of a set of conductive, equidistantly spaced electrodes mounted along the perimeter of a circular apparatus as shown in Fig. 1(a). The ECT sensing domain is defined as the circular area enclosed by the boundary electrodes. During ECT testing, an alternating current (AC) excitation is applied to one of the electrodes, while all others remain grounded, as shown in Fig. 1(b). This allows an electric field to propagate through the sensing domain. In addition, the electric field lines depend on the distribution of dielectric properties in the sensing domain, which affects the capacitance response at each boundary electrode. If permittivity distribution is known *a priori*, then the forward problem can be solved to compute the expected capacitance at the boundary electrodes. Experimentally though, capacitance is measured and used as inputs to the inverse problem for reconstructing the permittivity distribution of the sensing domain. The ECT forward and inverse problems are discussed next.

### A. Forward Problem

The forward problem utilizes a known spatial permittivity distribution and the 2D Laplace's equation to compute the capacitance response at the boundary electrodes:

$$\nabla \cdot (\varepsilon \nabla u) = 0 \tag{1}$$

where $\varepsilon$ is electrical permittivity, and $u$ is electric potential distribution. Here, it is assumed that no electrical source or sink is present inside the sensing domain ($\Omega$). Electrostatic approximation is imposed by setting the rotational component of the electric field ($E$) as zero [21]. Since (1) is a partial differential equation and is difficult to solve directly, finite element modeling (FEM) is employed to solve the weak form of

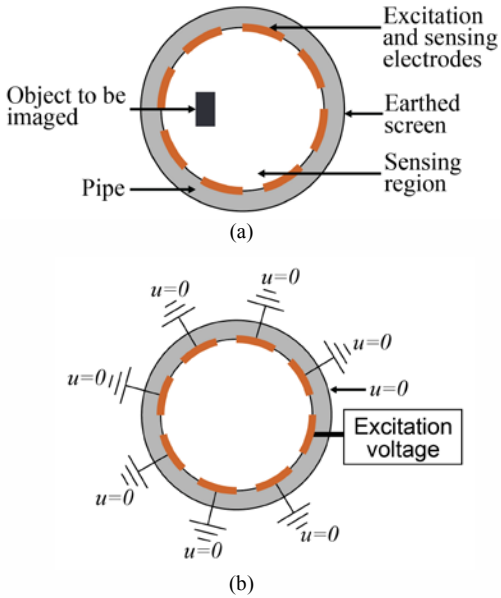


Fig. 1. (a) A schematic of the ECT test setup and (b) the interrogation scheme are shown.

(1), which can be obtained by multiplying it with a sufficiently smooth test function ($v$) and integrating over $\Omega$.

$$\int_{\Omega} v\nabla\cdot(\varepsilon\nabla u) = 0 \tag{2}$$

The boundary conditions of the ECT forward problem is defined such that the potential distribution of the excitation electrode (*i.e.*, the electrode used for AC signal injection) is equal to the magnitude of the excitation voltage. Since the other electrodes (*i.e.*, measurement electrodes) are grounded, their potential distribution is zero. Then, the electric potential ($u^h$) can be approximated as a linear combination of nodal values of electric potentials ($u_i$) and the nodal shape functions ($\phi_i$).

$$u^h = \sum_{i=1}^{n} u_i\phi_i \tag{3}$$

where $n$ is the total number of nodes in the FEM. In this study, three-node linear triangular elements were employed. Fig. 2 plots the potential distribution of a circular sensing domain when one electrode was injected with a 10 V signal.

Using (2) and by considering the appropriate boundary conditions, the result is a set of linear equations:

$$Ku = I \tag{4}$$

where $K$ is the system stiffness matrix obtained from the discrete representation of the operator, $\nabla\cdot(\varepsilon\nabla u)$, and $I$ is the force vector obtained from the boundary expressions. Then, the estimated values of $u$ can be used to calculate the capacitance ($C_{i,j}$) between the excitation ($i$) and measurement electrodes ($j$):

$$C_{i,j} = \frac{1}{V}\int_{e_j} \varepsilon\frac{\partial u_i}{\partial n}dl \quad i = 1:L;\ j = i+1:L \tag{5}$$

where $n$ is the unit inward normal to the $j^{\text{th}}$ measurement electrode of length $e_j$, $V$ is the magnitude of applied voltage, $L$ is the total number of electrodes, and $u_i$ is the solution of the forward problem when the $i^{\text{th}}$ electrode is used for excitation.

### *B. Inverse Problem*

The inverse problem seeks to reconstruct the spatial permittivity distribution of the sensing domain using the set of experimentally obtained boundary capacitance measurements ($C_m$). It should be mentioned that the same inverse problem was studied extensively for image reconstruction in electrical impedance tomography. Linear back projection algorithm [22], iterative Gauss-Newton, one step linear reconstruction [23-25], D-bar method [26], and constrained sine wave method [27], to name a few, were used by different groups for reconstructing conductivity distribution. In this study, Gauss-Newton iterative algorithm is developed for spatial permittivity reconstruction.

To jumpstart the inverse problem, the FEM of $\Omega$ is formulated assuming some spatial permittivity distribution. Let $F(\varepsilon)$ be the forward problem operator that can return the capacitance response at the boundary electrodes given a certain spatial permittivity distribution, $\varepsilon$, as the input. Then, an iterative Gauss-Newton algorithm is used for minimizing the error norm between $C_m$ and $F(\varepsilon)$ sets of capacitance. However, since the ECT inverse problem is ill-posed by nature, and changes in the permittivity distribution often result in just minute changes in boundary capacitance responses [21], the generalized Tikhonov regularization is adopted by adding a penalty term in the cost function ($p$) to be minimized as shown in (6).

$$p = \arg\min[\| F(\varepsilon) - C_m \|^2 + \alpha^2 \| R(\varepsilon - \varepsilon_o) \|^2] \tag{6}$$

where $\alpha$ and $R$ are the regularization parameter and regularization matrix, respectively, while $\varepsilon_o$ is the assumed background permittivity distribution. Here, (6) is solved using an iterative method. For the $i+1^{th}$ iteration step, permittivity ($\varepsilon_{i+1}$) can be estimated by linear approximation around the solution of the $i^{th}$ iteration step (*i.e.*, $\varepsilon_i$). By linearizing the problem based on the predicted values of permittivity distribution at the $i^{th}$ iteration, $\varepsilon_{i+1}$ can be expressed as:

$$\varepsilon_{i+1} = \arg\min[\| F(\varepsilon_i) + F'(\varepsilon_i)\Delta\varepsilon_i - C_m \|^2 + \alpha^2 \| R(\varepsilon_i + \Delta\varepsilon_i - \varepsilon_o) \|^2] \tag{7}$$

where $F'(\varepsilon_i)$ is the first derivative of $F(\varepsilon_i)$ with respect to $\varepsilon_i$. The difference of the predicted permittivity distribution between the $i+1^{th}$ and $i^{th}$ iterations (*i.e.*, $\Delta\varepsilon_i$) can be estimated in discrete form as follows:

$$\Delta\varepsilon_i = (J_i^T J_i + \alpha^2 R^T R)^{-1}\{J_i^T[C_m - F(\varepsilon_i)]\} + \alpha^2 R^T R(\varepsilon_o - \varepsilon_i) \tag{8}$$

where Jacobian matrix, $J_i$, is the discrete representation of $F'(\varepsilon_i)$ evaluated at the $i^{\text{th}}$ step. $R$ is taken to be the square root of the diagonal of the matrix $J_i^T J_i$. The main objective of regularization is to diminish the effect of smaller singular values in the solution of the inverse problem in an implicit way. The instability in the inverse algorithm can also be alleviated by regularization, since inclusion of the regularization terms in the cost function penalizes extreme changes in permittivity values to produce artificially smoother images. In this study, the regularization parameter $\alpha$ was estimated *a priori* and was equal to the variance of capacitance measurements.

The optimization scheme continues to execute until the error ratio ($e$) is greater than the specified threshold value of 0.05% (*i.e.*, the threshold established for this study), as shown in (9).

$$e = \frac{\| F(\varepsilon_i) - C_m \|^2}{\| C_m \|} \le 0.05\% \tag{9}$$

It should be mentioned that a good initial guess of the permittivity distribution can be used, which can drastically reduce the number of iterations required to satisfy the error threshold criterion. In this study, the initial distribution of the permittivity was assumed to be uniform and equal to the permittivity of air (*i.e.*, $8.85\times10^{-12}$ F/m).

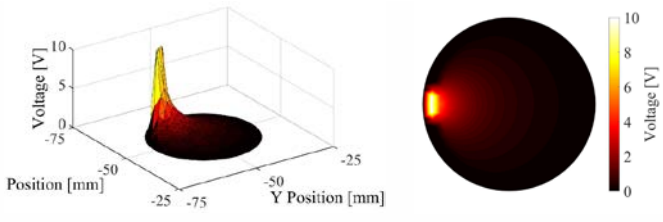


(a) (b)

Fig. 2. The potential distribution inside the sensing domain was computed by solving the forward problem, in this case, with a 10 V excitation signal.

### *C. Current State-of-the-Art*

A significant body of work related to electrical capacitance tomography has been reported. The first ECT hardware system was developed by Huang *et al.* [28], where an eight single-plane

electrode system was used for body scanning. A linear back projection algorithm was implemented for mapping permittivity distribution of two-component flow. Since then, ECT was successfully used for different industrial applications. Yang *et al.* [29] used ECT for detecting water droplet distribution in a gas-wet separator process. Dyakowski *et al.* [30] imaged and monitored the nylon polymerization process at an elevated temperature (~ 275 °C) and pressure (~ 22 bar). The dynamic behavior and temporal variations of electrical permittivity distribution of the system were analyzed from spatial permittivity distribution maps. Waterfall *et al.* [31] was able to use ECT for monitoring the combustion process inside a combustion engine. It was found that the combustion process triggers high volumes of electric charge that influences the electrical permittivity distribution inside the engine. ECT was also used for monitoring other industrial processes ranging from particulate process monitoring [32] to gas-solid cyclones [33] to more recently fluidized bed dryers [34, 35].

Beside those aforementioned industrial applications, ECT was also explored as a nondestructive evaluation tool (*e.g.*, for monitoring deposition inside buried pipes [36], damage detection in glass fiber-reinforced polymer composites [37], and subsurface damage detection in concrete [38], to name a few). Despite these advancements, the use of ECT for biomedical and healthcare remains fairly new but challenging. Although it was found that the dielectric properties of human cells can change due to infection [39], perhaps other means are also necessary to enhance the sensitivity of ECT to detect these dielectric changes.

## III. Experimental Details

As mentioned earlier, the objective was to advance ECT while incorporating passive nanocomposite sensing elements that can enhance detection sensitivity. First, the fabrication procedure of the MWCNT-PANI thin film pH sensor is discussed. Second, a parallel-plate capacitor-based test setup was devised for characterizing the sensitivity of its dielectric properties when the film was exposed to different pH buffer solutions. Third, the ECT algorithm and test setup was validated experimentally. Finally, after depositing the films onto a representative surrogate of an osseointegrated prosthesis, the specimen was exposed to different pH buffer solutions and subjected to ECT testing.

### *A. Nanocomposite pH Sensor Fabrication*

In recent years, medical imaging is significantly influenced by advancements in the nanotechnology domain. Nanomaterials' unique structure, size, shape, and resemblance to various molecules have made them suitable for biomedical applications. Examples are carbon nanotubes (CNT), silicon dioxide, boron nitride, titanium dioxide, and organic nanotubes. In particular, CNTs have received significant attention, where Li *et al.* [40] showed that the growth of osteoblastic cells could be accelerated by CNTs, which could produce extracellular matrix during formation of bone tissue. Hirata *et al*. [41] surface-coated MWCNTs onto 3D collagen scaffold for bone tissue engineering of primary osteoblasts of rats and observed more bone formation around the coated collagen sponge than uncoated ones.

On the other hand, a wide variety of polymers, such as polyaniline, are used with CNTs to encode desirable properties in nanocomposites for biomedical engineering [42]. It was shown that PANI could be used to produce a wide range of nanostructures when coupled with CNTs [43], and their use in biomedical applications has been recently investigated [43, 44]. Humpolicek *et al.* [45] studied the effects of PANI in the human body, where the conclusion was that it does not have any sensitization or skin irritation effects but could exhibit cytotoxicity. However, it was also reported that this cytotoxicity could be significantly reduced by a deprotonation and re-protonation procedure, which proves that cytotoxicity was not caused by PANI itself but by the reaction by-products. PANI could also be used as a sensor, where the electrical properties of PANI were demonstrated to exhibit pH sensitivity in aqueous environments [46]. In addition, previous work by Vandenberg and Loh [47] showed that the layer-by-layer technique was suitable for fabricating CNT-PANI thin film pH sensors, and different dopants could be used to tune its pH sensitivity.

In this work, an airbrushing technique [48] was adopted, since it is more time- and labor-efficient and can be easily scaled up for large-scale applications. Preparation of the ink solution for spraying involved two main steps. In the first step, 10 mg/mL solutions of polyaniline emeraldine base dissolved in N-N dimethyl formaldehyde (DMF) were prepared by stirring the mixture using a magnetic stirrer for 24 h. The resulting PANI-DMF solution was then vacuum-filtered using 0.45 μm membrane filters to eliminate undissolved particles. This was followed by a 10-fold dilution by adding appropriate amounts of deionized water, and its pH was adjusted to between 2.5 to 2.6 using 10 vol.% hydrochloric acid in deionized water.

For the second step, the final MWCNT-based ink was prepared. A detailed procedure for making the ink can be found in Gupta *et al.* [23]. In short, MWCNTs were mixed with 2 wt.% poly(sodium 4-styrenesulfonate) (PSS) solution and dispersed by ultrasonication. Thereafter, the MWCNT-PSS solution was mixed with the diluted and pH-adjusted PANI-based solution in equal proportions. The binder, which was a Kynar Aquatec latex solution, was then added to the solution to obtain the sprayable ink. Spray-coating was performed manually using a Paasche airbrush as illustrated in Fig. 3(a), and previous work showed that these MWCNT-based inks could be deposited onto a variety of substrates such as glass, plastics, metals, textiles, and fiber-reinforced polymer composites, among others [23-25, 49].

### *B. pH Sensing Characterization*

A simple parallel-plate capacitor arrangement was employed for characterizing how the dielectric properties of the MWCNT-PANI/latex thin films varied when exposed to different pH buffer solutions. First, Fig. 3(a) shows that thin film pH sensors were airbrushed onto one side of microscope glass slides. Conductive aluminum tape was affixed onto the other side of the film-coated slide. Another glass slide, with aluminum tape affixed onto one side of it, was also prepared. The two slides were then sandwiched together with the MWCNT-PANI/latex thin film in between the glass and the aluminum tape electrodes on the outside faces, as shown in Fig. 3(b). This setup created a parallel-plate capacitor, which is depicted in Figs. 3(c) and 3(d).

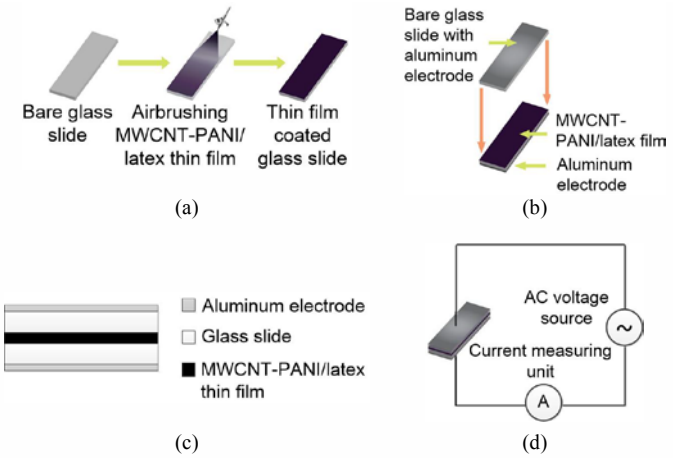


Fig. 3. (a) MWCNT-PANI/latex thin film was deposited onto glass slides by airbrushing. (b) The thin film was sandwiched between two glass slides with aluminum electrodes to (c) form a parallel-plate capacitor. (d) Testing involved measuring the current flow through the circuit.

It is known that the capacitance of a parallel-plate capacitor depends on its geometry and dielectric property between its two electrodes. It was hypothesized that pH would alter the electrical permittivity of the MWCNT-PANI/latex film. Since the geometry (*i.e.*, length and width of electrodes) was constant, any variations in measured capacitance would be due to dielectric property changes of the thin film alone. Here, the test began by disassembling the parallel-plate capacitor to expose the thin film, and a pH 1 buffer solution was pipetted onto its surface for 30 s and then dried using compressed air. Then, the parallel-plate capacitor was reassembled and subjected to capacitance testing, where the parallel plate-capacitor was excited using a 16 kHz, 10 V peak-to-peak, square-wave generated by an Agilent 33250A function generator. Instead of directly measuring capacitance, current in the circuit was measured using a Keysight 34460A digital multimeter and recorded using Keysight BenchVue data logging software, since it is directly proportional to capacitance. Fig. 3(d) illustrates the circuit and measurement setup. Capacitance was calculated by averaging 10,000 current measurements.

### *C. ECT Spatial Permittivity Mapping*

The final set of tests aimed to validate ECT and MWCNT-PANI/latex thin films for spatial permittivity reconstruction and for identifying changes in permittivity due to different pH. The measurement system consisted of eight 40 mm-long and equidistantly spaced electrodes. The sensing domain defined by these electrodes was a circular region with a diameter of 120 mm. In addition, a metallic shield on the outer surface of the electrodes was for eliminating electromagnetic interference that could potentially corrupt capacitance measurements. A high-performance capacitance data acquisition system was employed to measure the mutual capacitance between pairs of boundary electrodes. It should be mentioned that only independent measurements were used for ECT reconstruction (*i.e.*, 8×7/2=28 measurements). The electrodes were numbered consecutively in a counterclockwise direction, as shown in Fig. 4(a).

Using the ECT test setup, two sets of tests were performed.


(a) (b)

Fig. 4. (a) An eight electrode ECT measurement system was used. (b) An aluminum rod was used as a surrogate for a prosthesis, and it was coated with a pH-sensitive MWCNT-PANI/latex thin film and then wrapped with saturated foam to simulate human tissue.

The first set of experiments aimed to validate if the ECT algorithm and interrogation-acquisition system could detect the locations and shapes of objects placed in the sensing domain. Here, 25 mm-diameter aluminum rods were placed at different locations in the sensing domain, and the measured data were used for spatial permittivity reconstruction. Second, a lamb shank was also subjected to ECT testing to verify that ECT could resolve features of tissue versus bone and to demonstrate its merit for future implementations in human beings.

After system validation, ECT tests were conducted to simulate infection occurring at the tissue-prosthesis interface and to see if it was possible to detect changes in electrical permittivity due to pH (or infection). First, the ECT hardware was employed to obtain a set of boundary capacitance measurements when nothing was present in the sensing domain. This set of measurements would serve as the raw data used for computing the baseline permittivity distribution (of air). Second, a representative surrogate (or phantom) of an osseointegrated prosthesis was needed. In this case, a 25 mm-diameter aluminum rod was selected, followed by spray-coating a layer of insulating primer and then the MWCNT-PANI/latex thin film. The layer of insulating primer was deposited to electrically isolate the MWCNT-PANI/latex film from the rod. In reality, another biocompatible polymer coating could also be applied and will be investigated in future studies. Nevertheless, the phantom was then wrapped with foam, which was saturated with water, as shown in Fig. 4(b). The purpose of including the saturated foam was to simulate an environment similar to that of human tissue. The entire test setup is shown in Fig. 4(a).

To expose the film-coated phantom to pH buffer solutions, the film-coated rod was carefully removed without disturbing the saturated foam and then immersed in different pH buffer solutions. This was followed by drying the film-coated rod using compressed air and inserting it back into the cylindrical saturated foam layer so that the entire system was in the same location in the sensing domain as before. At this point, the sensing domain was interrogated, and boundary capacitance measurements were recorded. This procedure was repeated using the same film-coated prosthesis phantom, where, in total, the system was exposed to pH 1 to 13 buffers, in increments of 2. Lastly, changes in spatial permittivity were obtained by comparing each result with respect to the reconstructed permittivity distribution of the baseline (of just air).

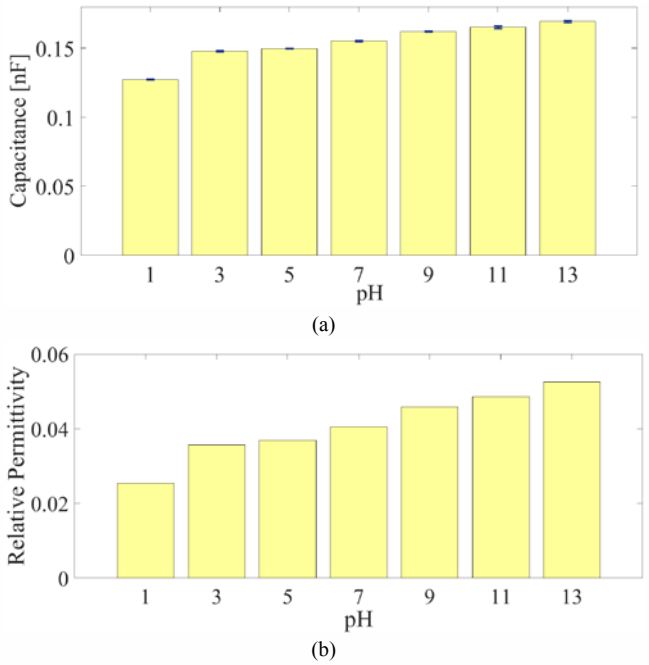


Fig. 5. The permittivity of the MWCNT-PANI/latex film changed as the film was exposed to different pH buffer solutions, which changed the (a) measured capacitance of the test setup. Standard deviations of measured capacitance are also shown (for 10,000 measurements). (b) The relative permittivity of the film, corresponding to different pH, was computed.

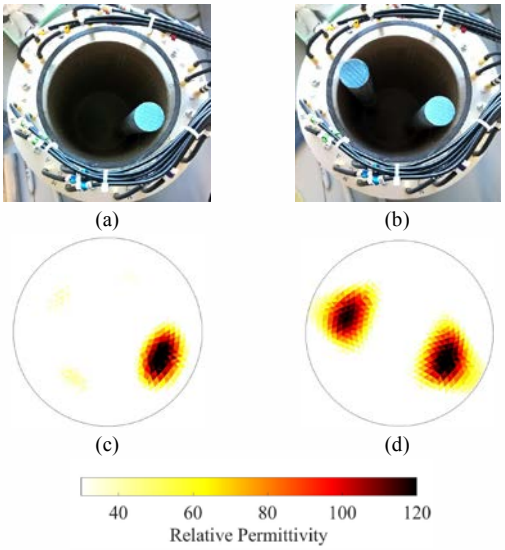


Fig. 6. (a) Aluminum rods were placed in the sensing domain near electrode-8 and (b) on the opposite side. (c) The corresponding ECT permittivity maps successfully identified the rod near electrode-8 and (d) when both of them were simultaneously present in the sensing domain.

## IV. Experimental Results and Discussion

### A. Thin Film pH Sensing

As was described in Section III.B, MWCNT-PANI/latex thin films exposed to different pH buffer solutions were sandwiched between two aluminum electrodes and glass slides to create a parallel-plate capacitor test setup. Fig. 5(a) plots a representative set of capacitance results with respect to different pH, where the error bars correspond to the standard deviation of each dataset. It can be observed that capacitance increases in tandem with increasing pH. Since the geometry of the parallel-plate capacitor was fixed, it can be concluded that the electrical permittivity of MWCNT-PANI/latex thin films increased with increasing pH. In addition, using known dimensions of the test setup and by estimating the permittivity of glass as 4.7, the thin film's relative permittivity when exposed to different pH buffers could be calculated and plotted, as presented in Fig. 5(b). In order to estimate the electrical permittivity of the thin film, it was assumed that each layer of the dielectric materials (*i.e.*, glass and MWCNT-PANI/latex thin film) acted as separate dielectric materials that were connected in series. It should be mentioned that the thickness of similar spray-coated MWCNT-based films were determined by scanning electron microscopy and was ~ 10 μm [48], which was also assumed here.

### B. ECT Validation

In order to validate the ECT algorithm, a series of experiments were conducted by placing aluminum rods at different locations in the sensing domain, as was described in Section III.C and shown in Figs. 6(a) and 6(b). A 25 mm-diameter aluminum rod was placed near electrode-8, followed by another near electrode-4, as shown in Figs. 6(a) and 6(b), respectively; Fig. 4(a) shows the electrode numbering scheme. Then, ECT measurements were collected. The introduction of the aluminum rod would result in localized changes in the permittivity distribution, which would in turn affect the propagation of the induced electric field. Similarly, the corresponding spatial permittivity maps were solved. It should be noted that absolute reconstructed permittivity values were converted into relative permittivity by dividing them with the electrical permittivity of free space (*i.e.*, $8.85\times10^{-12}$ F/m), and the relative permittivity distributions are shown. It can be observed that sharp changes in localized relative permittivity can be observed where the aluminum rods were placed. These results were observed for both of the cases with one and two rods, where the relative permittivity distribution for the case of two rods is shown in Fig. 6(d).

Overall, it can be concluded that the size and locations of the aluminum rods were accurately captured using ECT. The results presented in Fig. 6 successfully validated the ECT algorithm and measurement scheme. Previous work also showed that ECT was able to characterize the simultaneous presence of different materials within the sensing domain [50, 51].

### C. Tissue and Bone ECT Imaging

After validating ECT (Section IV.B), a simple experiment was conducted using a lamb shank as the specimen to demonstrate that ECT has the potential for imaging tissue and bone (and in the future, human beings). The lamb shank, as shown in Fig. 7(a), was placed in the ECT sensing domain and interrogated, followed by reconstructing its change in relative permittivity distribution with respect to an empty sensing domain as the baseline. It can be seen from Fig. 7(b) that the shape of the lamb shank was successfully captured by ECT. In addition, greater changes in permittivity were also observed near the vicinity of the bone, while the remainder of the permittivity changes were due to the presence of tissue. Although Fig. 7 is only a

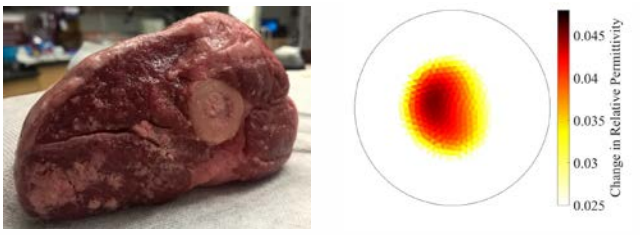


(a) (b)

Fig. 7. (a) A lamb shank was used for ECT testing, and (b) the relative change in permittivity map successfully identified the bone and tissue regions that corresponded to the lamb shank specimen.

preliminary validation of this technique for use in biological systems, the result shown in Fig. 7(b) is promising.

*D. Noncontact pH Sensing*

After validating the potential of ECT for imaging bone and tissue, this study continued with investigating whether ECT could noninvasively identify pH changes as an indication of infection occurring at tissue-prosthesis interfaces. Prosthesis phantoms pre-coated with MWCNT-PANI/latex thin films were used for the next set of tests. A rod was wrapped in foam saturated in deionized water (*i.e.*, to simulate the simultaneous presence and properties of human tissue), as shown in Fig. 4. ECT was performed on the film-coated rod prior to it being exposed to pH buffers, and the resulting relative permittivity distribution is presented in Fig. 8(a).

From Fig. 8(a), one can identify three distinct regions of different electrical permittivity. First, the center portion of highest relative permittivity (of ~ 120) corresponded to the prosthesis phantom. Second, a large ring with a relative permittivity of ~ 80 can be seen, whose value is close to that of deionized water, and its size is comparable to the experimental setup. Last, the outermost region is air. While metals are characterized by infinite electrical permittivity, ECT and FEM are unable to reconstruct this but instead converges to a large number. In addition, regularization inherently smooths sharp edges (*e.g.*, the interface between the foam and air) to show a gradient of change in relative permittivity. Fig. 8(b) shows that the ECT algorithm could converge at ~ 125 iterations when the error threshold reaches 0.01% (*i.e.*, the threshold set in this case), and negligible changes in error threshold is observed after ~ 200 iterations. In general, Fig. 8 successfully validated that ECT was able to reconstruct the absolute relative permittivity of

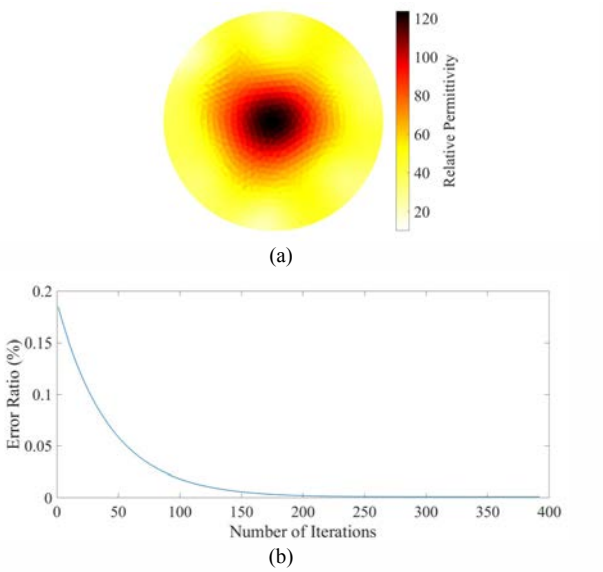


(a)

(b)

Fig. 8. (a) The ECT relative permittivity distribution reconstruction of a film-coated phantom rod wrapped in saturated foam is shown. (b) The plot shows the number of iterations required for the algorithm to converge to different error thresholds.

materials in its sensing domain (*i.e.*, to within a reasonable degree of accuracy given estimation and experimental errors).

The next test involved exposing the film-coated rod to pH buffer solutions. As discussed in Section III.C, the film-coated rod was immersed in a pH 1 buffer solution, dried using compressed air, and placed back in the saturated foam. The entire tissue-prosthesis surrogate was centered in the sensing domain as shown in Fig. 4(a). Boundary capacitance measurements (*i.e.*, mutual capacitance between the boundary electrode pairs) were obtained, and the raw data was used as inputs for solving the ECT inverse problem and for obtaining its respective relative permittivity distribution. As discussed in Section III.C, this procedure was repeated using the same phantom rod for pH 3, 5, 7, 9, 11, and 13 buffers. The permittivity map for an empty sensing domain was employed as the baseline, and the relative change in permittivity distributions for all the pH cases were computed with respect to this baseline.

The ECT permittivity maps for one set of tests are shown in Fig. 9. First, it can be observed from Fig. 9 that ECT successfully identified the location of the prosthesis phantom, and it compares well with its actual location shown in Fig. 4(a); the

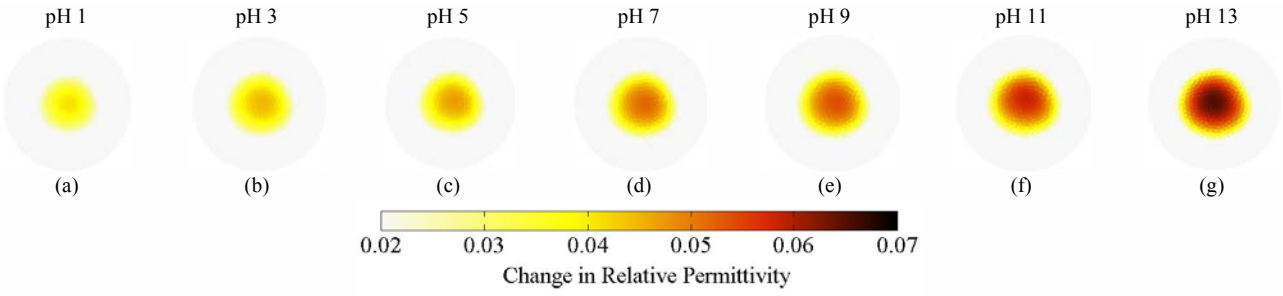


Fig. 9. The film-coated rod (*i.e.*, prosthesis phantom) was exposed to pH (a) 1, (b) 3, (c) 5, (d) 7, (e) 9, (f) 11 and (f) 13 buffer solutions, and the corresponding reconstructed change in permittivity distributions with respect to the baseline (*i.e.*, the empty sensing domain case) are shown.

film-coated phantom was located in the center of the sensing domain. Similarly, since the remainder of the sensing domain was air throughout the entire set of tests, the reconstructed permittivity maps do not show any permittivity changes there, but a comparatively small change in permittivity can be observed around the prosthesis phantom. It is anticipated that this change was caused due to the presence of saturated foam.

Second, one can also observe changes in localized electrical permittivity due to the application of different pH buffer solutions. This result was only possible with the introduction of the MWCNT-PANI/latex thin film on the prosthesis phantom, since it was already demonstrated in Section IV.A and Fig. 5 that the film's electrical permittivity was sensitive to pH. As expected, the ECT permittivity maps shown in Fig. 9 also confirmed that permittivity increased with increasing pH. Overall, these results suggest that ECT, when used in conjunction with pH-sensitive thin films, can potentially serve as a noninvasive tool for monitoring pH (as a precursor for infection occurring near tissue-prosthesis interfaces). Future tests will consider the embedment of a prosthesis surrogate in tissue and bone samples while conducting simulated infection tests.

## V. Numerical Simulations and Results

Given that the results presented in Section IV.D confirmed that ECT was able to monitor changes in pH in a noninvasive fashion, numerical simulations were performed to further explore the capabilities of ECT. The goal was to characterize whether ECT could detect highly localized changes in electrical permittivity (*i.e.*, to effectively model the case when infection was only occurring at a portion of the tissue-prosthesis interface). Realism was introduced during modeling by also taking into account measurement noise.

### *A. Numerical Model*

Fig. 10 illustrates the numerical model considered in this section. The sensing domain was a circular region (similar to before) with a radius of 50 mm. For simplicity, it was assumed that the ECT hardware could fit tightly over the limb of an amputee so that the entire sensing domain contained human tissue (with no air); ECT permittivity mapping would be conducted on the cross-section of the limb where the actual hardware would be attached. The relative permittivity of tissue was modeled as 50 [52]. In addition, the osseointegrated prosthesis was modeled as a metallic rod with a relative permittivity of 150 and a radius of 25 mm, as shown in Fig. 10(a). While Fig. 10(a) shows the pristine tissue-prosthesis system, Fig. 10(b) illustrates the case when infection started to develop. Unlike Section IV.D where the entire interface was exposed to pH buffer solutions to simulate infection, only 25% of the tissue-interface was assumed to be infected. Because different types of infection could potentially alter the pH of human tissue (as well as the permittivity of the MWCNT-PANI/latex films) differently, both localized decreases and increases in electrical permittivity were investigated. Here, relative permittivity changes of the quarter-circle region were introduced with approximately comparable magnitudes as

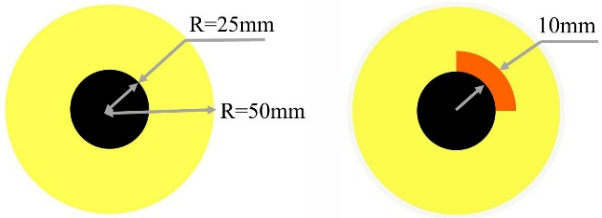


Fig. 10. (a) The numerical model considered a circular cross-section prosthesis bar embedded in human tissue. (b) Infection was simulated by altering the electrical permittivity value of the highlighted region in orange.

observed in the experimental results due to a unit change in pH. First, the permittivity of the highlighted (orange) quarter-circle infected region in Fig. 10(b) was assumed to decrease from 50 (*i.e.*, uninfected or pristine tissue) to 49.9 and then to 49.8. Second, the permittivity of the infected region was also increased from 50 to 50.1 to 50.2.

For the ECT FEM, the system consisted of 12 electrodes, each 25 mm-wide, and were arranged in a circular array equidistant from one another. During each ECT interrogation, a 10 V AC electric field was propagated between the excitation and measurement electrodes. The forward problem was solved, and this resulted in a total of 12×11/2=66 independent boundary capacitance results. The computed capacitance values were corrupted with Gaussian white noise whose amplitude was 1% of the median of the estimated capacitance distribution. Noise was introduced to simulate measurement uncertainty as if experiments were conducted. Thereafter, the corrupted capacitance data were used as inputs to the ECT inverse problem for electrical permittivity distribution reconstruction.

### *B. Localized Infection Results*

The simulation results are shown in Fig. 11. As mentioned earlier, relative permittivity was initially decreased by 0.20 at the infected quarter-circle region. The forward problem was then executed to estimate the boundary capacitance, followed by the inclusion of Gaussian white noise, and used for permittivity reconstruction by ECT. The change in relative permittivity maps were computed using a baseline of the pristine system (*i.e.*, metallic prosthesis with a relative permittivity of 150 fully embedded in uninfected tissue of relative permittivity equal to 50). The result when the relative permittivity of the infected region decreased by 0.20 is presented in Fig 11(a). The same procedure was repeated but for relative permittivity values of the infected region as 49.9, 50.1, and 50.2, and the corresponding results are shown in Figs. 11(b), 11(c), and 11(d), respectively.

First, it can be observed that the change in relative permittivity distributions shown in Fig. 11 only show highly localized changes corresponding to where infection was simulated. In addition, Fig. 11 also confirmed that ECT was able to capture both decreases and increases in localized permittivity; the magnitude of permittivity change also compared well with the assigned values. Second, for the remaining uninfected regions, no major changes in relative permittivity were observed. While localizing infection may not be as critical as detecting its presence, the results shown in Fig. 11 suggest that ECT has the

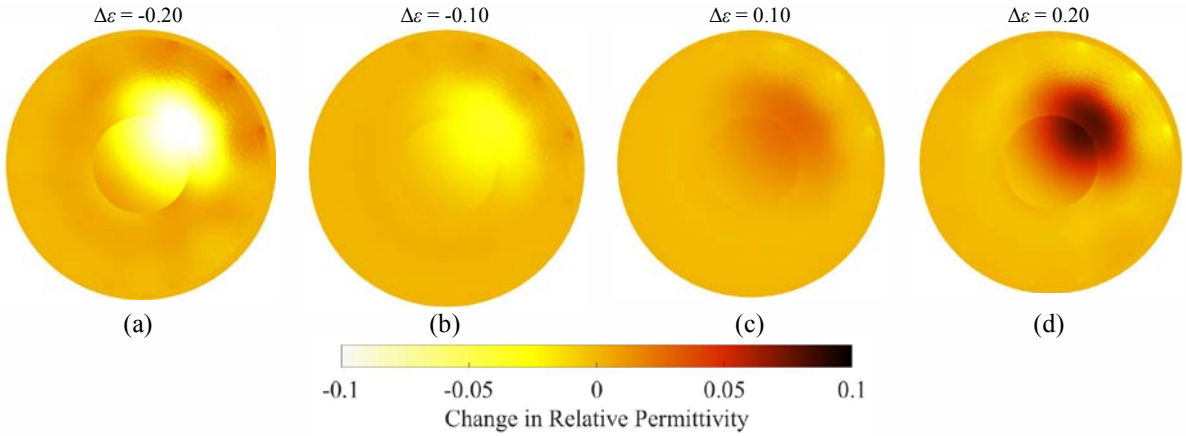


Fig. 11: The change in relative permittivity maps (with respect to the baseline of a metallic prosthesis embedded in uninfected tissue) of simulated localized infected were computed by assigning the infected region with a relative permittivity of (a) 49.80, (b) 49.90, (c) 50.10, and (d) 50.20.

potential for identifying early stages of infection, where only a portion of the tissue-prosthesis interface was affected. Future work will validate these results experimentally, as well as to consider more complicated scenarios and more realistic prosthesis phantoms embedded in tissue-like materials.

## VI. Conclusions

A noncontact, noninvasive, capacitance-based tomographic imaging technique was proposed in this study for monitoring infection occurring at tissue-prosthesis interfaces. Infection due to various microorganisms changes the localized pH of human tissue. For this reason, an MWCNT-PANI/latex thin film whose electrical permittivity was sensitive to pH was designed and fabricated. A parallel-plate capacitor test arrangement was devised, and the film's capacitance was measured as it was subjected to different pH buffer solutions. It was found that its electrical permittivity increased as the film was exposed from pH 1 to 13 buffer solutions. Since the objective was to detect and monitor subcutaneous infection, direct measurements were not possible, and electrical capacitance tomography was employed. The system was validated for identifying, in a noncontact fashion, the location of aluminum rods placed inside the sensing domain defined by a circular ring of noncontact electrodes. In addition, ECT could also image the cross-section of a lamb shank, thereby demonstrating its potential for imaging tissue and bone. Upon validating the system, a representative replica of an osseointegrated prosthesis was created, and the pH-sensitive MWCNT-PANI/latex thin film was spray-coated onto the rod. To simulate infection occurring at the tissue-prosthesis interface, the prosthesis phantom was exposed to different pH buffer solutions. ECT was then used to interrogate the system and to reconstruct the electrical permittivity distribution maps.

The experimental results showed that ECT successfully identified the location of the prosthesis phantom, as well as changes in permittivity due to exposure of its pre-coated film to different pH. Finally, a set of numerical simulations was also performed to see if ECT could detect highly localized infection. The simulation results, while considering a small level of measurement uncertainty, was able to capture localized changes in electrical permittivity induced by infection. These results suggest that the system has potential for use as a noninvasive, noncontact, subcutaneous, infection monitoring and diagnostic tool, particularly, for patients who have osseointegrated prostheses and implants. Future research will assess the biocompatibility and cytotoxicity of the nanocomposite. This will be followed by characterizing the magnitude of changes in pH when infection occurs in living tissue. Infection monitoring and animal studies will also be investigated.

## Acknowledgements

This research was supported by the Office of Naval Research (ONR) under Contract No. N00014-17-1-2550. It was also supported by the Jacobs School of Engineering, University of California-San Diego. The authors would also like to thank Ms. Bo Mi Lee for her assistance with preparing illustrations for this manuscript.

## References

[1] K. Ziegler-Graham, E. J. MacKenzie, P. L. Ephraim, T. G. Travison, and R. Brookmeyer. (2008). Estimating the prevalence of limb loss in the United States: 2005 to 2050. *Archives of Physical Medicine and Rehabilitation. 89(3)*, pp. 422-429.

[2] M. F. Owings and L. J. Kozak. (1998). Ambulatory and inpatient procedures in the United States, 1996. *Vital and Health Statistics. Series 13, Data from The National Health Survey. 139*, pp. 1-119.

[3] D. J. Stinner, T. C. Burns, K. L. Kirk, C. R. Scoville, J. R. Ficke, and J. R. Hsu. (2010). Prevalence of late amputations during the current conflicts in Afghanistan and Iraq. *Military Medicine. 175(12)*, pp. 1027-1029.

[4] H. Fischer. (2010). US military casualty statistics: operation new dawn, operation Iraqi freedom, and operation enduring freedom. Congressional Research Service. Washington, DC.

[5] Healthcare Cost Utilization Project. HCUP: a federal-state-industry partnership in health data sponsored by the Agency for Healthcare Research and Quality. (2012).

[6] R. Adell, B. Eriksson, U. Lekholm, P. I. Brånemark, and T. Jemt. (1990). Long-term follow-up study of osseointegrated implants in the treatment of totally edentulous jaws. *The International Journal of Oral and Maxillofac Implants. 5(4)*, pp. 347-359.

[7] R. Branemark, O. Berlin, K. Hagberg, P. Bergh, B. Gunterberg, and B. Rydevik. (2014). A novel osseointegrated percutaneous prosthetic system for the treatment of patients with transfemoral amputation: A prospective study of 51 patients. *The Bone and Joint Journal. 96(4)*, pp. 562-562.

[8] A. Khemka, L. Frossard, S. Lord, B. Bosley, and M. Al Muderis, "Osseointegrated prosthetic limb for amputees: over hundred cases," in

Proceedings of 6th International Conference Advances in Orthopaedic Osseointegration, Nevada, 2015.

[9] H. Van de Meent, M. T. Hopman, and J. P. Frölke. (2013). Walking ability and quality of life in subjects with transfemoral amputation: a comparison of osseointegration with socket prostheses. *Archives of Physical Medicine and Rehabilitation. 94(11)*, pp. 2174-2178.

[10] J. Tillander, K. Hagberg, L. Hagberg, and R. Brånemark. (2010). Osseointegrated titanium implants for limb prostheses attachments: infectious complications. *Clinical Orthopaedics and Related Research. 468(10)*, pp. 2781-2788.

[11] W. Zimmerli. (2006). Prosthetic-joint-associated infections. *Best Practice and Research Clinical Rheumatology. 20(6)*, pp. 1045-1063.

[12] A. J. Tande and R. Patel. (2014). Prosthetic joint infection. *Clinical Microbiology Reviews. 27(2)*, pp. 302-345.

[13] M. Müller, L. Morawietz, O. Hasart, P. Strube, C. Perka, and S. Tohtz. (2008). Diagnosis of periprosthetic infection following total hip arthroplasty–evaluation of the diagnostic values of pre-and intraoperative parameters and the associated strategy to preoperatively select patients with a high probability of joint infection. *Journal of Orthopaedic Surgery and Research. 3(31)*, pp. 1-8.

[14] Y. C. Wong, Q. J. Lee, Y. L. Wai, and W. F. Ng. (2005). Intraoperative frozen section for detecting active infection in failed hip and knee arthroplasties. *The Journal of Arthroplasty. 20(8)*, pp. 1015-1020.

[15] B. L. Atkins, N. Athanasou, J. J. Deeks, D. W. Crook, H. Simpson, T. E. Peto, P. McLardy-Smith, A. R. Berendt, and O. C. S. Group. (1998). Prospective evaluation of criteria for microbiological diagnosis of prosthetic-joint infection at revision arthroplasty. *Journal of Clinical Microbiology. 36(10)*, pp. 2932-2939.

[16] J. G. Hughes, E. A. Vetter, R. Patel, C. D. Schleck, S. Harmsen, L. T. Turgeant, and F. R. Cockerill. (2001). Culture with BACTEC Peds Plus/F bottle compared with conventional methods for detection of bacteria in synovial fluid. *Journal of Clinical Microbiology. 39(12)*, pp. 4468-4471.

[17] C. Love, S. E. Marwin, and C. J. Palestro. (2009). Nuclear medicine and the infected joint replacement. *Seminars in Nuclear Medicine. 39(1)*, pp. 66-78.

[18] T. C. Kwee, R. M. Kwee, and A. Alavi. (2008). FDG-PET for diagnosing prosthetic joint infection: systematic review and metaanalysis. *European Journal of Nuclear Medicine and Molecular Imaging. 35(11)*, pp. 2122-2132.

[19] R. R. Marples, D. T. Downing, and A. M. Kligman. (1971). Control of free fatty acids in human surface lipids by Corynebacterium acnes. *Journal of Investigative Dermatology. 56(2)*, pp. 127-131.

[20] M. Soleimani and W. R. Lionheart. (2005). Nonlinear image reconstruction for electrical capacitance tomography using experimental data. *Measurement Science and Technology. 16(10)*, pp. 1987-1996.

[21] M. Soleimani, "Image and shape reconstruction methods in magnetic induction and electrical impedance tomography," Ph.D. Thesis, University of Manchester, Manchester, England, 2005.

[22] F. Santosa and M. Vogelius. (1990). A backprojection algorithm for electrical impedance imaging. *SIAM Journal on Applied Mathematics. 50(1)*, pp. 216-243.

[23] S. Gupta, J. G. Gonzalez, and K. J. Loh. (2016). Self-sensing concrete enabled by nano-engineered cement–aggregate interfaces. *Structural Health Monitoring. 16(3)*, pp. 309-323.

[24] K. J. Loh, T. C. Hou, J. P. Lynch, and N. A. Kotov. (2009). Carbon nanotube sensing skins for spatial strain and impact damage identification. *Journal of Nondestructive Evaluation. 28(1)*, pp. 9-25.

[25] B. R. Loyola, T. M. Briggs, L. Arronche, K. J. Loh, V. La Saponara, G. O'Bryan, and J. L. Skinner. (2013). Detection of spatially distributed damage in fiber-reinforced polymer composites. *Structural Health Monitoring. 12(3)*, pp. 225-239.

[26] E. K. Murphy, J. L. Mueller, and J. C. Newell. (2007). Reconstructions of conductive and insulating targets using the D-bar method on an elliptical domain. *Physiological measurement. 28(7)*, pp. S101-S114.

[27] T. N. Tallman and K. Wang. (2016). Damage and strain identification in multifunctional materials via electrical impedance tomography with constrained sine wave solutions. *Structural Health Monitoring. 15(2)*, pp. 235-244.

[28] S. Huang, A. Plaskowski, C. Xie, and M. Beck. (1989). Tomographic imaging of two-component flow using capacitance sensors. *Journal of Physics E: Scientific Instruments. 22(3)*, pp. 173-177.

[29] W. Yang, A. Chondronasios, S. Nattrass, V. Nguyen, M. Betting, I. Ismail, and H. McCann. (2004). Adaptive calibration of a capacitance tomography system for imaging water droplet distribution. *Flow Measurement and Instrumentation. 15(5)*, pp. 249-258.

[30] T. Dyakowski, T. York, M. Mikos, D. Vlaev, R. Mann, G. Follows, A. Boxman, and M. Wilson. (2000). Imaging nylon polymerisation processes by applying electrical tomography. *Chemical Engineering Journal. 77(1)*, pp. 105-109.

[31] R. Waterfall, R. He, N. White, and C. Beck. (1996). Combustion imaging from electrical impedance measurements. *Measurement Science and Technology. 7(3)*, pp. 369-374.

[32] W. Zhang, C. Wang, W. Yang, and C.-H. Wang. (2014). Application of electrical capacitance tomography in particulate process measurement-a review. *Advanced Powder Technology. 25(1)*, pp. 174-188.

[33] H. G. Wang, Liu Shi and F. Y. Wu Qiang. (2006). 3D Imaging with Electrical Capacitance Tomography In Cyclone Separators. *Journal of Engineering Thermophysics. 27(1)*, pp. 177-179.

[34] S. Liu, Q. Chen, H. Wang, F. Jiang, I. Ismail, and W. Yang. (2005). Electrical capacitance tomography for gas–solids flow measurement for circulating fluidized beds. *Flow Measurement and Instrumentation. 16(2)*, pp. 135-144.

[35] H. Wang, T. Dyakowski, P. Senior, R. Raghavan, and W. Yang. (2007). Modelling of batch fluidised bed drying of pharmaceutical granules. *Chemical Engineering Science. 62(5)*, pp. 1524-1535.

[36] E. Al Hosani, M. Zhang, and M. Soleimani. (2015). A limited region electrical capacitance tomography for detection of deposits in pipelines. *IEEE Sensors Journal. 15(11)*, pp. 6089-6099.

[37] X. Yin and D. A. Hutchins. (2012). Non-destructive evaluation of composite materials using a capacitive imaging technique. *Composites Part B: Engineering. 43(3)*, pp. 1282-1292.

[38] X. Yin, D. Hutchins, G. Diamond, and P. Purnell. (2010). Non-destructive evaluation of concrete using a capacitive imaging technique: preliminary modelling and experiments. *Cement and Concrete Research. 40(12)*, pp. 1734-1743.

[39] B. B. Abraham and G. Anitha. (2012). Designing of lab view based electrical capacitance tomography system for the imaging of bone using NI ELVIS and NI USB DAQ 6009. *Bonfring International Journal of Power Systems and Integrated Circuits. 2(2)*, pp. 1-6.

[40] X. Li, H. Gao, M. Uo, Y. Sato, T. Akasaka, S. Abe, Q. Feng, F. Cui, and F. Watari. (2009). Maturation of osteoblast-like SaoS2 induced by carbon nanotubes. *Biomedical Materials. 4(1)*, pp. 1-8.

[41] E. Hirata, M. Uo, H. Takita, T. Akasaka, F. Watari, and A. Yokoyama. (2011). Multiwalled carbon nanotube-coating of 3D collagen scaffolds for bone tissue engineering. *Carbon. 49(10)*, pp. 3284-3291.

[42] J. Stejskal, I. Sapurina, and M. Trchová. (2010). Polyaniline nanostructures and the role of aniline oligomers in their formation. *Progress in Polymer Science. 35(12)*, pp. 1420-1481.

[43] E. N. Konyushenko, J. Stejskal, I. Šeděnková, M. Trchová, I. Sapurina, M. Cieslar, and J. Prokeš. (2006). Polyaniline nanotubes: conditions of formation. *Polymer International. 55(1)*, pp. 31-39.

[44] L. P. Wang, W. Wang, L. Di, Y. N. Lu, and J. Y. Wang. (2010). Protein adsorption under electrical stimulation of neural probe coated with polyaniline. *Colloids and Surfaces B: Biointerfaces. 80(1)*, pp. 72-78.

[45] P. Humpolicek, V. Kasparkova, P. Saha, and J. Stejskal. (2012). Biocompatibility of polyaniline. *Synthetic Metals. 162(7)*, pp. 722-727.

[46] B. Adhikari and S. Majumdar. (2004). Polymers in sensor applications. *Progress in Polymer Science. 29(7)*, pp. 699-766.

[47] A. Vandenberg and K. J. Loh. (2012). Evaluating the pH sensitivity of carbon nanotube-polyaniline thin films with different dopants. *Nano LIFE. 2(4)*, pp. 1-12.

[48] L. P. Mortensen, D. H. Ryu, Y. J. Zhao, and K. J. Loh. (2013). Rapid assembly of multifunctional thin film sensors for wind turbine blade monitoring. *Key Engineering Materials Journal. 569-570*, pp. 515-522.

[49] L. Wang, S. Gupta, K. J. Loh, and H. S. Koo. (2016). Distributed Pressure Sensing Using Carbon Nanotube Fabrics. *IEEE Sensors Journal. 16(12)*, pp. 4663-4664.

[50] S. Gupta and K. J. Loh. (2017). Non-contact tomographic imaging and nanocomposite films for monitoring human-prosthesis interfaces. *Procedia Engineering. 188*, pp. 110-118.

[51] S. Gupta and K. J. Loh, "Characterization and localization of sub-surface structural features using non-contact tomography," In *Proceedings of the ASME 2016 Smart Materials, Adaptive Structures, and Intelligent Systems (SMASIS) Conference*, 2016, Stowe, VT.

[52] W. T. Joines, Y. Zhang, C. Li, and R. L. Jirtle. (1994). The measured electrical properties of normal and malignant human tissues from 50 to 900 MHz. *Medical Physics. 21(4)*, pp. 547-550.